Two-Dimensional Copper Nanosheets for Electrochemical Reduction of Carbon Monoxide to Acetate

Wesley Luc[1,2,†], Xianbiao Fu[1,†], Jianjian Shi[3], Jing-Jing Lv[2], Matthew Jouny[2], Byung Hee Ko[2], Yaobin Xu[4], Qing Tu[4], Xiaobing Hu[4], Jinsong Wu[4], Qin Yue[1], Yuanyue Liu[3], Feng Jiao[2,*], Yijin Kang[1,*]

1. *Institute of Fundamental and Frontier Sciences, University of Electronic Science and Technology of China, Chengdu, Sichuan 610054, China*

2. *Center for Catalytic Science and Technology, Department of Chemical and Biomolecular Engineering, University of Delaware, Newark, Delaware, USA*

3. Texas Materials Institute and Department of Mechanical Engineering, The University of Texas at Austin, Austin, Texas 78712, USA

4. *Department of Materials Science and Engineering, Northwestern University, Evanston, Illinois 60208, USA*

† *These authors contributed equally.*

Corresponding author: jiao@udel.edu, kangyijin@uestc.edu.cn

Abstract

Upgrading carbon dioxide to high-value multi-carbon (C_{2+}) products is one promising avenue for fuel and chemical production. Among all monometallic catalysts, copper has attracted much attention because of its unique ability to convert CO_2 or CO to C_{2+} products with an appreciable selectivity. While numerous attempts have been made to synthesize Cu materials that expose desired facets, it still remains a challenge to obtain high-quality nanostructured Cu catalysts for electroreduction of CO_2/CO. Herein, we report a facile synthesis of freestanding triangular-shaped two-dimensional Cu nanosheets, that selectively expose the (111) surface. In a 2M KOH electrolyte, the Cu nanosheets exhibit an acetate Faradaic efficiency of 48% with an acetate partial current density up to 131 mA cm^{-2} in electrochemical CO reduction. Further analysis suggest that the high acetate selectivity is attributed to the suppression of ethylene and ethanol formation, likely due to the reduction of exposed (100) and (110) surfaces.

Introduction

Carbon dioxide electrolysis process powered by renewable electricity at decreasing price is an attractive approach for the sustainable production of fuels and chemicals because this process uses greenhouse CO_2 gas rather than fossil sources as the carbon feedstock.[1-10] To achieve a high-performing CO_2 electrolysis process, efficient CO_2 electrocatalysts are required to minimize the energy barriers for CO_2 activation. Among all the existing CO_2 electrocatalysts, copper is one of the most widely studied material because it is able to convert CO_2 (or CO_2-derived carbon monoxide) to multi-carbon (C_{2+}) products at relatively high selectivities in comparison to other monometallics.[1-6,9,11-16] Many efforts have been devoted toward engineering Cu-based catalysts, such as nanostructuring, thermal annealing, and alloying, in the hopes of steering product selectivity and boosting catalytic activity. Although some progresses have been made, a good understanding of the structure-activity relationship is still lacking in Cu-catalyzed CO_2/CO electroreduction, which is mainly due to the difficulties in synthesizing well-defined Cu materials with surfaces terminated with desired facets. For example, the well-defined Cu (111) model surface at nanoscale is still missing, while the Cu (100) has been offered by solution-phase-synthesized Cu nanocubes.[17-20]

Recently we have shown that micron-sized and oxide-derived Cu (OD-Cu) catalysts are able to reduce CO to C_{2+} products at high rates in an alkaline electrolyte.[3] Among all the C_{2+} products, acetate with a Faradaic efficiency of ~20% was observed, which is higher than what is typically observed in CO_2 electroreduction (<5%).[3,14] Transport modeling suggests a highly alkaline environment (a high pH value) near the electrode-electrolyte interface may promote the formation of acetate.[3] However, it is still unclear whether the surface nature of the catalyst also plays a role in enhancing acetate production. Because of the polycrystalline nature of both catalysts, correlating the observed acetate selectivity with the catalytic surface structure is difficult. Therefore, new synthetic methods for engineering Cu nanomaterials with well-controlled surfaces are urgently required.

Herein, we report the synthesis of freestanding high-quality Cu nanosheets with two-dimensional (2D) triangular shaped morphology using a solution-phase-synthesis procedure. The as-synthesized Cu nanosheets are ~5 nm thick, which selectively exposed Cu {111} facets. As a model catalyst for CO electroreduction, the Cu nanosheets exhibit an acetate Faradaic efficiency as high as 48%, representing the among highest acetate selectivity that has been achieved in electrochemical CO_2/CO electroreduction at practical rates of reaction (>100 mA cm^{-2}). The enhanced acetate formation is attributed to the suppression of other C_{2+} products, due of the reduction of exposed (100) and (110) surfaces that are known to be favorable toward ethylene and ethanol formation. Furthermore, computation studies suggest that the pathway toward acetate formation goes through a ketene intermediate, with the incorporation of one oxygen atom from the electrolyte and the other originating from the CO reactant.

Results

Synthesis of Cu nanosheets. The 2D Cu nanosheets were synthesized through a chemical reduction of copper(II) nitrate by L-ascorbic acid in the presence of hexadecyltrimethylammonium bromide (CTAB) and hexamethylenetetramine (HMTA). Transmission electron microscope (TEM) image (Figures 1a) reveals that the as-synthesized Cu nanosheets are triangular with an average edge length of ~1.7 ± 0.5 μm. The high resolution TEM (HRTEM) image shows the projection of the basal plane exhibiting angles of ~60° between fringes (Figure 1b). The hexagonal pattern seen in HRTEM as well as in the selective area electron diffraction (SAED) can be attributed to either 1/3{422} of the *fcc* structure along the [111]

direction (Figure 1c, inset) or (100) of the *hcp* structure along the [001] direction.[21] However, further analysis with X-ray diffraction (XRD, Figure 1c and Supplementary Figure 1) confirmed that the structure of the Cu nanosheets is *fcc* and not *hcp*. Note that, the 1/3{422} reflections of an *fcc* structure should be forbidden; however, exceptions may exist for non-3*n* layers with thicknesses within a few nanometers.[21] The substantially enhanced (111) peak shown in the XRD pattern (Figure 1c), which was obtained from assembling the nanosheets on a Si wafer, indicates that the preferentially oriented {111} planes were parallel to the Si substrate. The fringe distances of 0.15 nm and 0.13 nm as shown in Figure 1b closely match the Cu {112} and Cu {220} lattice distances, respectively. This suggests that the projection seen in the HRTEM image (Figure 1b) is indeed {111} in the <111> direction. In the region where two nanosheets overlapped, a Moire pattern can be seen directly in the HRTEM image (Figure 1d) as well as in the corresponding fast Fourier transform (FFT) pattern (Figure 1e). The observed secondary pattern in the FFT pattern further confirms the presence of {111} basal planes. The atomic force microscopy (AFM) line scan (Figure 1f) reveals that the thickness of the Cu nanosheets is ~5 nm. With these observations, it was concluded that the as-synthesized Cu nanosheets are ultra-thin and enclose by two {111} basal planes. In addition, Cu nanocubes that selectively expose {100} facets as the Cu (100) model surface were also synthesized by a modified method as previously reported.[20] TEM image (Figure 1g) shows an edge length of 41.4 ± 3.6 nm, and the HRTEM image (Figure 1h) confirms the presence of {100} planes by the cubic arrangement of Cu atoms. The fringe distance of 0.18 nm matches the lattice spacing of Cu {200}. The XRD pattern (Figure 1i) of the preferentially oriented Cu nanocubes shows an enhanced (200) peak, further indicating the dominant {100} planes.

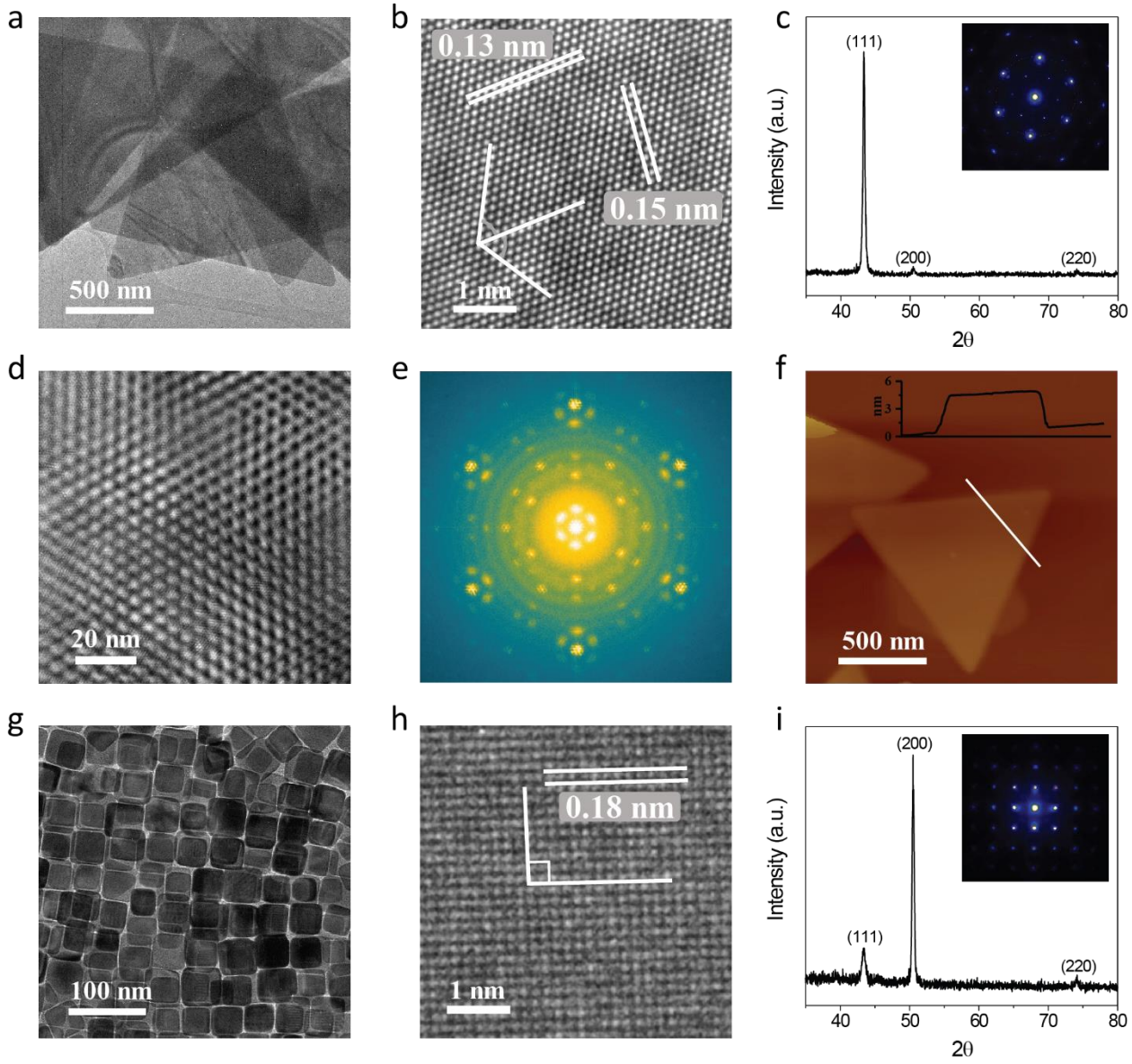

Figure 1. Characterization of Cu nanosheets and Cu nanocubes. a) TEM image of triangular Cu nanosheets; b) HRTEM image showing the basal plane projection of a Cu nanosheet; c) XRD pattern of Cu nanosheets assembled on a Si wafer, preferentially showing the (111) peak, inset of c) SAED pattern of Cu nanosheets; d) HRTEM image and e) corresponding FFT pattern showing a Moire pattern from two overlapped Cu nanosheets; f) AFM image showing the thickness of a single Cu nanosheet; g) TEM image and h) HRTEM image of Cu nanocubes; and i) XRD pattern of Cu nanocubes assembled on a Si wafer, preferentially showing (200) peak, inset of i) SAED pattern of Cu nanocubes. Scale bars: a, f) 500nm, b, h) 1 nm, d) 20nm, and g) 100 nm.

The combination of appropriate reducing agent, ligand, and surfactant was the key for the successful synthesis of {111}-enclosed Cu nanosheets (Supplementary Figure 2). As a long-life reducing agent, L-ascorbic acid not only reduces Cu (II) to Cu (0) via Cu(I), but also protects the final product from oxidation.

The as-synthesized Cu nanosheets exhibited a red color (Supplementary Figures 3a, 4, and 5) which suggests the presence of Cu (0), and the observed liquid-crystal-like texture was the result of stacking of nanosheets. Such appearance remained unchanged for at least four months under ambient conditions (Supplementary Figure 4). However, Cu nanoparticles were completely oxidized within one hour (Supplementary Figures 3c and 3d), as indicated by a red-to-blue color change. Diffuse reflectance infrared Fourier transform spectroscopic (DRIFT) measurement (Supplementary Figure 6) shows the presence of ascorbic acid in the Cu nanosheets sample. It is likely that surface absorbed ascorbic acid is responsible for the improved chemical stability. Although ascorbic acid was used as the surfactant, an acidic environment is not preferred during synthesis as the Cu nanocrystal growth cannot be controlled. The cuprous ions easily disproportionate in an acidic solution, resulting in an uncontrolled rate of reduction. To provide an alkaline environment, CTAB and HMTA were both used to stabilize the cuprous ion in the aqueous solution. By doing so, the coordination number of the cuprous ion was three and the coordination geometry was trigonal planar, which directed the anisotropic growth of the Cu nanosheets.

With an edge length of ~1.7 μm and a thickness of ~5 nm, theoretically, at least 99% of the exposed surface (*i.e.* basal planes) should be (111). As shown in scanning electron microscope (SEM) and TEM images (Supplementary Figures 7a and 7b), the majority of the nanosheet (shadowed area) has a single-crystal morphology with {111} basal plane while the edges are polycrystalline and oxidized. This was confirmed with X-ray photoelectron spectroscopy (XPS), as the as-synthesized Cu nanosheets show partial oxidization to Cu (II) (Supplementary Figure 7d). The single-crystal region remained intact even after CO electroreduction; however, the oxidized region corroded away (Supplementary Figure 7c). This was also confirmed by post-reaction XPS as majority of the Cu is in its reduced state. Slight oxidation was observed likely due to sample handling after CO electroreduction experiments. These observations indicate that the most striking feature of the Cu nanosheets have extraordinarily stable (111) surface, and such a stable zero-valence Cu (111) surface is crucial for catalysis studies. As surface reconstruction is well known[22,23] (i.e. the oxidation/reduction cycles may change the atomic arrangement of metal surfaces), it is difficult to obtain Cu (111) directly from reducing CuO (111) or Cu_2O (111).

CO electroreduction performance. The CO electroreduction properties of Cu nanosheets were evaluated using a three-compartment flow-cell electrolyzer. As described in previous works,[3,11,24-27] the use of a flow-cell electrolyzer enables high-rate of CO conversion (>100 mA cm^{-2}) which cannot be typically achieve with conventional batch reactors due to the low solubility limitation of CO in aqueous electrolytes. The CO electroreduction performances in 0.5-2M KOH electrolyte are summarized in Figure 2a and Supplementary Figures 8 and 9. The current densities increased near-exponentially with increasing applied potentials, indicating that the mass transport limitation of CO was minimal. In 2M KOH, a maximum C_{2+} products Faradaic efficiency of ~70% was achieved with the major C_{2+} products being ethylene and acetate with minor amounts of ethanol and n-propanol. At more negative potentials, small amount of methane was produced. Interestingly, a maximum acetate Faradaic efficiency of ~48% (Figure 2a) and an acetate partial current density up to 131 mA cm^{-2} were achieved in 2M KOH (Figure 2c), among the highest reported to date toward acetate formation. The CO electroreduction performances are tabulated in Supplementary Table 1. The stability of Cu nanosheets was also examined under a constant current of 100 mA cm^{-2} for 3 hours in 2M KOH (Figure 2b). The results show a stable acetate Faradaic efficiency over the span of the stability test, except for the first 30 min, which could be caused by initial activation of catalyst layer. The oscillation of the potential is due to bubble accumulation and sudden flush out in the cathode chamber during

electrolysis. *Operando* X-ray absorption spectroscopy (XAS) was also used to investigate the structural change of the Cu nanosheets under CO electroreduction conditions in a flow-cell electrolyzer (Supplementary Figure 10). Both the X-ray absorption near-edge spectroscopy (XANES) and extended X-ray absorption fine structure (EXAFS) spectrums (Supplementary Figure 11) show that the catalyst was in its metallic Cu^0 state and appear similar throughout the reaction, further confirming the structural stability of the catalyst.

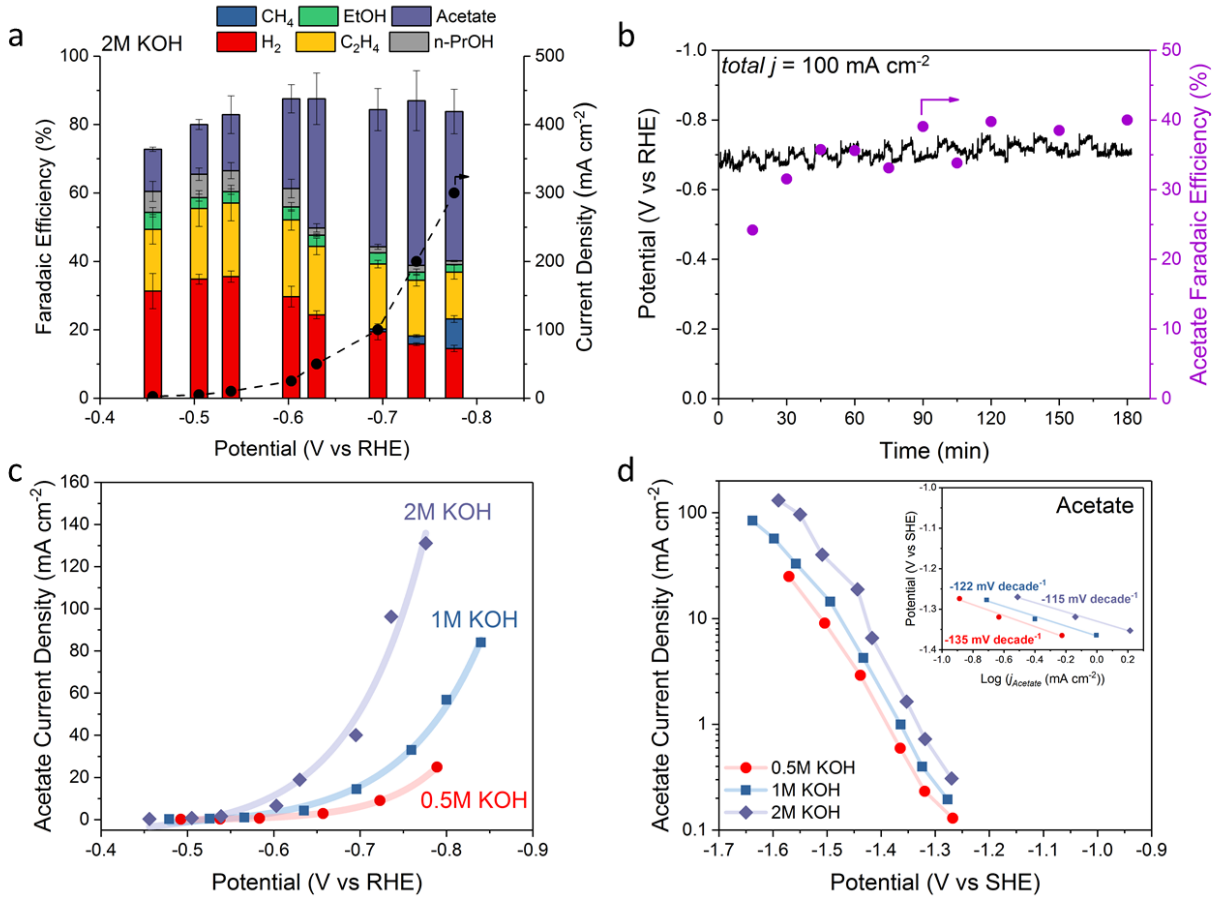

Figure 2. CO electroreduction performance of Cu nanosheets. a) Total current density and Faradaic efficiencies vs. applied potential for CO electroreduction on Cu nanosheets in 2M KOH. b) Stability test over a span of 3-hour electrolysis in 2M KOH. c) The acetate production performance on copper nanosheets in various KOH concentrations. d) Acetate partial current density and inset) Tafel analysis on the SHE scale. Error bars represent the standard deviation from at least three independent measurements and Tafel lines were determined with linear fit.

To examine the influence of pH on acetate formation in CO electroreduction, the acetate partial current densities in different electrolytes (0.5-2M) were plotted against the absolute potential scale (SHE), and Tafel slopes were derived from the three lowest partial current densities (Figure 2d). The other electroreduction products are shown in Supplementary Figure 12. Low current densities were chosen to obtain Tafel slopes as accurately as possible, since at higher current densities, significant amount of gas products was produced which can cause voltage fluctuation. It must be noted that Tafel analyses have

limitations and are typically done at low overpotentials and low currents to avoid mass transport limitation caused by not only the transport of reactant to the catalytic surface, but also by the adsorption of cations.[28] From Figure 2d, it is clear that acetate production has a strong pH dependence. As the hydroxide ion concentration increased, a positive shift in onset potential for acetate and a change to lower Tafel slopes (Figure 2d, inset) were observed, indicating that acetate formation is favored in highly alkaline environments. $C^{18}O$ labeling studies (Supplementary Figure 13) on Cu nanosheets show that the produced acetate in the form of acetic acid is partially-labeled where one oxygen of the acetate is originated from the CO feed and the other oxygen is originated from the electrolyte as consistent with previous studies,[3,29] further supporting that acetate formation is strongly dependent on the alkalinity of the electrolyte. Ethanol, n-propanol, and acetaldehyde were also detected (Supplementary Figures 11, b-d), and the labeling results were similar to our previous work.[3] Kanan and co-workers have also observed an enhancement in acetate formation, accompanied with a decrease in ethanol, at high pH on oxide-derived Cu and have attributed to the attack of a hydroxide ion to a surface-bound ketene or other carbonyl-containing intermediate.[9] The formation of hydrogen and ethylene are insensitive to the changes in pH (Supplementary Figure 12), as consistent with other reports;[16,30-32] while ethanol has a small pH dependence at low overpotentials.

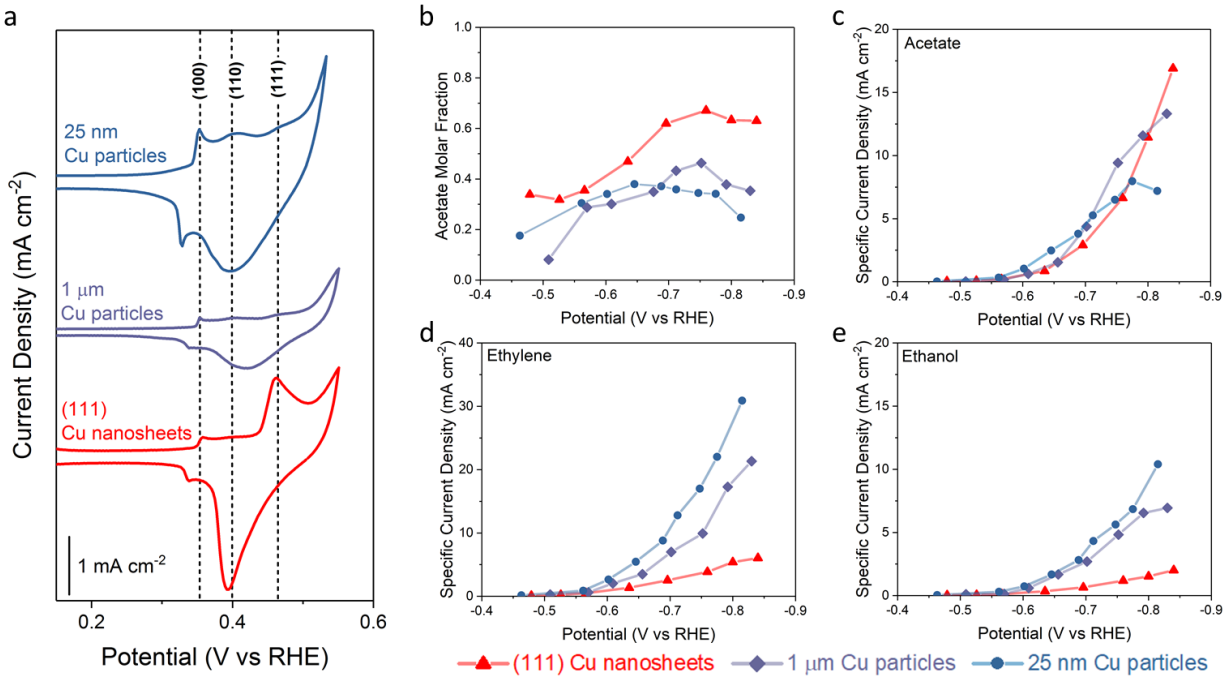

Figure 3. Comparison of copper nanosheets with commercial copper particles in 1M KOH. a) Voltammograms of OH_{ads} peaks collected in Ar-purged 1M KOH batch cell. b) Acetate molar production fraction excluding hydrogen. c-e) ECSA corrected acetate, ethylene, and ethanol partial current densities of various Cu catalysts, respectively.

To further understand the high acetate selectivity of Cu nanosheets, CO electroreduction was performed on commercial 1 μm and 25 nm Cu particles (Supplementary Figure 14) with a similar catalyst loading of 0.5 mg cm^{-2}, and the catalytic performances were compared. Electrosorption of hydroxide (OH_{ads}) was first used to probe the surface structure of the commercial Cu particles and Cu nanosheets.[33,34] Qualitatively, the

Cu nanosheets have a pronounced (111) OH_{ads} feature, suggesting a high surface density of (111). As for the commercial particles, the (100), (110), and (111) OH_{ads} peaks are similar in relative intensities, reflecting the polycrystalline surface nature of the commercial particles. *In-situ* OH_{ads} studies on the Cu nanosheets were also conducted in the flow-cell electrolyzer prior to and immediate after CO electrolysis by switching the gas feed to avoid potential oxidation during sample handling. The pre- and post-reaction voltammograms (Supplementary Figure 15) show similar features, indicating that the high surface density of (111) was preserved and that the catalytic performance of the Cu nanosheets is not attributed to surface reconstruction. In comparison to the commercial Cu particles, the Cu nanosheets have a higher acetate molar production fraction (excluding hydrogen) in the similar potential region, indicating that the Cu nanosheets are more selective toward converting CO to acetate (Figure 3b). To further compare the reaction rates, the performances (Supplementary Figures 16 and 17) were normalized to the electrochemical surface area (ECSA; see Supplementary Figure 18 for measurement). Surprisingly, the trend in specific acetate current density of the Cu nanosheets is similar to commercial Cu particles (Figure 3c), suggesting that all Cu catalysts have similar intrinsic activity toward acetate formation. However, the intrinsic activities toward ethylene and ethanol formation are much lower on the Cu nanosheets than commercial Cu particles (Figure 4d and 4e). To rule out the effects of ascorbic acid, which was critical for the successful synthesis of the Cu nanosheets, commercial 25 nm Cu particles were treated with ascorbic acid and tested for CO electroreduction. The performance of the treated Cu particles (Supplementary Figure 19) is similar to the untreated Cu particles, demonstrating that ascorbic acid has a minimal effect on catalytic performance. With these observations, we therefore attribute the overall enhancement of acetate formation on Cu nanosheet to the suppression of ethylene and ethanol formation. Previous single-crystal studies on CO electroreduction have shown that the (111) surface is unfavorable for the formation of ethylene and ethanol; while, (100) and (110) surfaces are more favorable.[35,36] The Cu nanosheets selectively expose {111} surfaces, theoretically 99% of the as-synthesized surface is (111), which reduce the overall surface density of (100) and (110). This consequentially suppresses ethylene and ethanol formation while enhancing the overall selectivity toward acetate. However, to the best of our knowledge, the mechanistic understanding of acetate on Cu surfaces has yet been fully elucidated and further work is needed. In addition, Cu nanocubes with exposed {100} surfaces exhibits similar CO electroreduction performance (Supplementary Figure 20) as the 25 nm commercial Cu particles.

DFT calculations. To understand the acetate formation pathway on Cu surfaces, density functional theory (DFT) calculations were performed and the calculation details can be found in Methods. Based on the isotopic labelling studies, H_2O incorporation must be involved during acetate formation to introduce ^{16}O. As *CO-COH (* denotes a binding site) is known be a common intermediate proposed in literature for the formation of C_{2+} products,[37-40] we focused our calculations from this initial intermediate. It must be noted that the pathway toward acetic acid, the protonated form of acetate, was determined such that the intermediate species are charge neutral. Starting from *CO-COH, acetic acid may form through: *CO-COH + H_2O+ e^- → *C-CO + H_2O + OH^-, *C-CO + H_2O + e^- → *CH-CO + OH^-, *CH-CO + H_2O + e^- → *CH_2-CO + OH^-, *CH_2-CO + H_2O → CH_3-COOH (Figure 4a). Note that in alkaline conditions, no protons are available for reaction, and thus, water is likely the proton donator.[32] This pathway involves the water incorporation into ethenone (CH_2-CO), a ketene specie, to form acetic acid (CH_3-COOH), and the DFT calculations of the free energy evolutions show that this pathway is thermodynamically feasible (Figure 4b). In addition, the barrier for water incorporation into the ketene is only 0.61 eV (Supplementary Figure 21), suggesting it is also kinetically feasible. We also found that ethenone is weakly adsorbed on Cu surfaces

with a binding energy of 0.06 eV for (111) and 0.21 eV for (100); therefore, the water incorporation into the ketene specie to form acetic acid is less affected by the difference in Cu surfaces, explaining its weak surface dependence. Lastly, acetic acid may also form without involving a ketene as the intermediate, through: *CH-CO + H_2O → *CH_2-COOH, *CH_2-COOH + H_2O + e^- → CH_3-COOH + OH^- (Supplementary Figure 22). However, calculations show that this pathway has a higher energy barrier for water incorporation (0.76 eV, Supplementary Figure 21). Therefore, the formation pathway involving ethenone, the ketene specie, is more likely. As OH^- ions are more nucleophilic than H_2O, it is likely that OH^- ions also interact with the ketene intermediate to form acetate; however, the computation assessment of charged species is currently difficult. The alcohol pathway (Figure 4a) shares a common *CH-CO intermediate with the acetic acid pathway and this could explain the competitive formation of ethanol and acetate that have been previously observed.[9] The *CH-CO intermediate was proposed by Calle-Vallejo and Koper as a possible intermediate toward C_{2+} products,[40] and our calculations show that the pathway toward ethanol through *CH-CO is thermodynamically feasible (Supplementary Figure 23). To further elucidate the influence of pH, future work should also focus on calculating the kinetic barriers of each step as a function of pH, as the pH could affect the overall pathways toward various C_{2+} products.

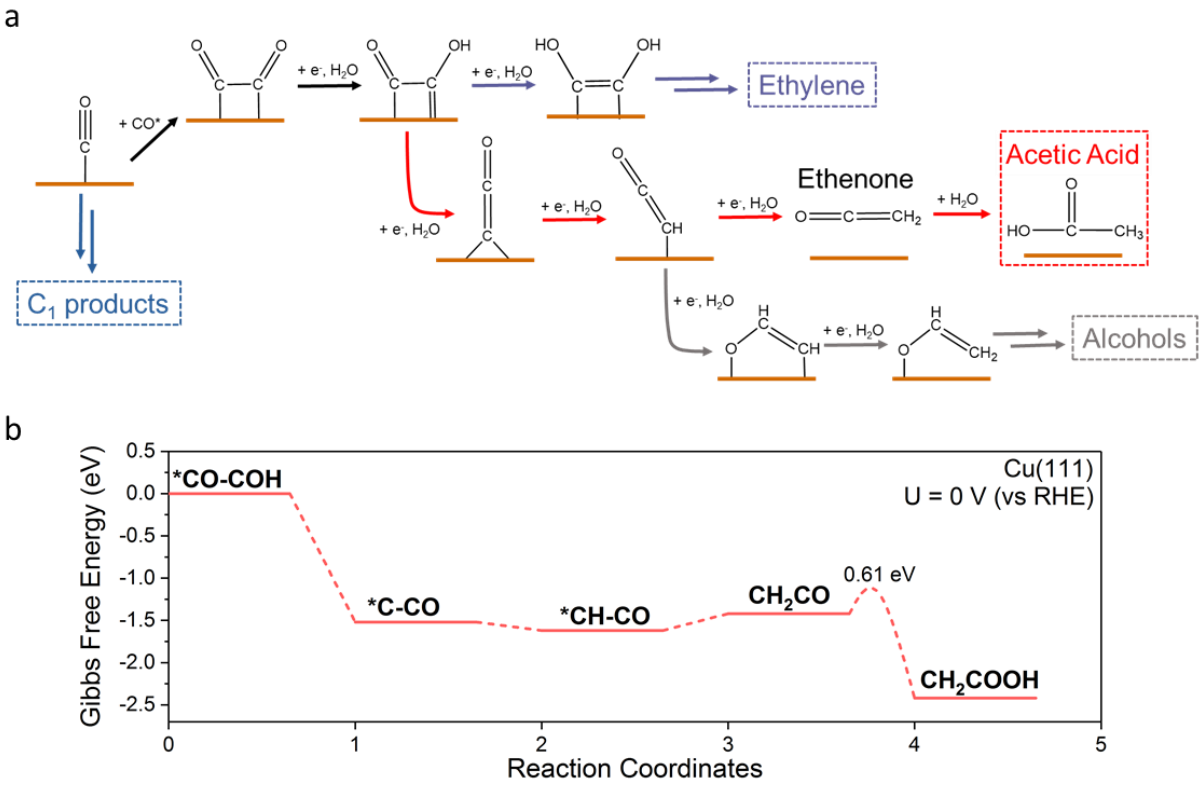

Figure 4. DFT calculations. a) Proposed mechanism for the electroreduction of CO to C_{2+} products. b) Energy evolution for acetic acid formation on Cu (111) at 0 V (vs RHE).

As described in previous reports,[41] multiple beneficial properties can be added up toward one catalytic process. In this paper, we demonstrated that a highly selective CO-to-acetate conversion can be achieved solely by materials engineering. Very recently, Kanan and co-workers developed an electrolyzer (*i.e.* through chemical reactor engineering) utilizing an interdigitated flow field that can produce highly

concentrated acetate product (~1.1M) using a proton-exchange membrane (Nafion).[2] Therefore, a design incorporating materials engineering and reactor engineering may push the acetate conversion to the level that is economically viable. For instance, an electrolyzer design can be explored by utilizing Cu nanosheets with an anion-exchange membrane at a maximal local alkalinity near the catalytic interface to further boost acetate production.

Methods

Synthesis of copper nanosheets

In a typical synthesis of Cu nanosheets, copper(II) nitrate trihydrate ($Cu(NO_3)_2 \cdot 3H_2O$, 50 mg), L-ascorbic acid (100 mg) and 15.0 mL deionized water were added into a vial (volume: 20 mL). After forming a homogeneous solution, hexadecyltrimethylammonium bromide (100 mg) and hexamethylenetetramine (100 mg) were added. After 30 min stirring, the vial of solution was capped and heated from room temperature to 80 °C (~2 °C/min) and kept at 80 °C for 3 h in an oil bath. The resulting products were collected by centrifugation and washed three times with an ethanol/deionized water mixture.

Synthesis of copper nanocubes

In a typical synthesis of Cu nanocubes, 35.0 mL oleylamine and 3.0 g trioctylphosphine oxide were mixed at room temperature and were heated to 60 °C (~5 °C/min) under vacuum. After kept at 60 °C for 20 min, the vacuum was replaced by Ar atmosphere, and 215.0 mg CuBr was rapidly added into the mixture. The solution was then heated 265 °C (~7 °C/min) and kept for 20 min before naturally cooling to room temperature. The resulting products were collected by centrifugation and washed three times with hexane/ethanol.

Preparation of electrodes

To construct the cathode electrode, a catalyst slurry containing 25 mg of as-synthesized Cu nanosheets, 3 mL isopropanol, and 20 µL of Nafion ionomer solution (5 wt% in H_2O) was first mixed and sonicated. Next, the catalyst slurry was slowly dropcast onto a Sigracet 29 BC GDL (Fuel Cell Store) to achieve a catalyst loading of ~0.5 mg cm^{-2}. A similar procedure was used to for commercial 1 µm Cu particles (0.5-1.5 µm, 99%; Alfa Aesar) and 25 nm Cu particles (25nm nanopowder; Sigma-Aldrich). As for the anode electrode, IrO_2 nanoparticles (99%; Alfa Aesar) was used instead.

Material Characterization

TEM images were taken with a Hitachi 8100 at an acceleration voltage of 200 kV. High-resolution TEM images were taken with a JEOL ARM300F at an acceleration voltage of 200 kV. AFM measurements were performed on a Dimension Icon (Bruker) to obtain 3D profiles of the patterns. XRD spectra were collected on a Rigaku SmartLab Thin-film Diffraction Workstation with a Cu Kα source. A high intensity 9 kW copper rotating anode x-ray source is coupled to a multilayer optic. An Auriga 60 Cross Beam scanning electrode microscopy (SEM) instrument was used to obtain SEM images of the copper nanosheets. To analyze the composition near the surface, a K-Alpha X-ray Photoelectron Spectrometer System (Thermo Fisher Scientific) was used. CasaXPS software was used to analyze the XPS data and conduct peak analysis. The adventitious carbon peak was calibrated to 284.5 eV and all peaks were fitted using a Gaussian/Lorentzian product line shape with a Shirley background.

The ECSA was determined by measuring the double-layer capacitance (C_{DL}) of the as-prepared electrodes in Ar-purged 0.1M $HClO_4$ in a H-cell. The scan rate was varied from 10 to 100 mV sec^{-1} in the non-Faradaic potential region and the observed current was plotted as a function of scan rate to obtain the C_{DL}. The ECSA was determining by normalizing the C_{DL} to that of a copper foil.

OH_{ads} studies were conducted by performing cyclic voltammetry in an Ar-purged 1M KOH in a H-cell. The voltammogram was collected at 100 mV sec^{-1}. I*n-situ* OH_{ads} studies was conducted by flowing Ar in the flow-cell electrolyzer. The electrolyte flow rate was stopped to minimize the fluctuation in the voltammogram. Next, CO electrolysis was conducted at constant current density of 100 mA cm^{-2} for one hour by switching the gas feed to CO and flowing the electrolyte. Immediately after electrolysis, the gas feed was switch back to Ar, the electrolyte flow rate was stopped, and then cyclic voltammetry was performed.

Operando XAS was performed at the 8-ID Beamline of the National Synchrotron Light Source II at Brookhaven National Laboratory. A modified two-compartment flow-cell electrolyzer made from acrylic was used for *operando* XAS studies (Supplementary Figure 10). The gas chamber had a small window cut out sealed with Kapton film to allow fluorescence signals to pass from the electrode to the detector. XAS data were processed using the IFEFFIT package, including ATHENE and ARTEMIS.[42]

Flow-cell CO electrolysis

CO reduction was conducted in a three-chamber flow cell as previously described. The dimension of the flow channels was 2 cm × 0.5 cm × 0.15 cm. The CO gas flow rate was controlled using a mass flow controller (MKS GE50) and set to 15 sccm. Aqueous potassium hydroxide solution (99.99%; Sigma-Aldrich) was used as both the catholyte and the anolyte. Peristaltic pumps were used to control the flow rate of the electrolytes at ~0.5 to 2 mL min^{-1}. A hydroxide exchange membrane (FAA-3; Fumatech) was used to separate the cathode and anode chambers. The gas outlet backpressure of the flow cell was modulated to atmospheric pressure with a backpressure controller (Cole-Parmer).

Electrolysis experiments were conducted using chronopotentiometry with a potentiostat (Autolab PGSTAT204). The cathode potentials were measured against an external Ag/AgCl reference electrode (Pine Research), and the solution resistance between the reference electrode and the cathode was measured using a current-interrupt technique before each electrolysis experiment. The measured potential was converted to the RHE scale using E (versus RHE) = E (versus Ag/AgCl) + 0.210 V + 0.0591 × pH and was iR-corrected. For each current density, products were quantified over a period of 200 s and at least three replicates were conducted to get an average and standard deviation.

During electrolysis, gas products were quantified using an in-line Multiple Gas Analyzer gas chromatography system (SRI Instruments) equipped with a HayeSep D and Molsieve 5 A columns connected to a thermal conductivity detector (TCD) and a flame ionization detector (FID). Argon (99.999%) was used as the carrier gas. Liquid products were analyzed using a Bruker AVIII 600 MHz NMR spectrometer. In short, 500 µL of sampled catholyte was mixed with 100 µL D_2O containing 20 ppm (*m/m*) dimethyl sulphoxide (≥99.9%; Alfa Aesar) as the internal standard. The one-dimensional ^1H spectrum as measured with water suppression using a pre-saturation method.

Labelled $C^{18}O$ experiment

Labelling studies were conducted with a $C^{18}O$ lecture bottle (95 at% ^{18}O; Sigma Aldrich). In short, $C^{18}O$ gas was extracted using a 30 mL syringe and a syringe pump was used to control the feed rate into the flow cell. The feed rate was set to 5 mL min^{-1}. Constant current electrolysis was conducted at 300 mA cm^{-2} for 5 min and the liquid product was collected for analysis. The liquid products were slightly acidified to a pH value of ~2 using hydrochloric acid to allow detection of acetate as acetic acid. Mass spectrum analysis was conducted with an integrated GC-MS (Agilent 59771A) system equipped with a DB-FFAP column and a mass spectrometry system (Agilent 59771A). Mass fragmentation patterns, focused on the parent ion of the molecules, were compared with those of the National Institute of Standards and Technology library.

Computational Methods

DFT calculations were performed using the Vienna Ab-initio Simulation Package (VASP)[43,44] with PAW pseudopotential[45] and the Perdew-Burke-Ernzerhosf (PBE) exchange-correlation functional[46]. The Cu (111) surface is modelled by a 4 × 4 slab with 4 layers, and (100) surface is modelled by a 4 × 4 slab with 3 layers (Supplementary Figure 24). The slabs are separated by ~ 15 Å from its periodic images. We used 3×3×1 Monkhorst Pack[47] k-points, and a kinetic energy cut-off of 400 eV. All atomic positions were fully relaxed until the final force on each atom being less than 0.01 eV/Å. The free energy of the solid system was calculated by adding the adsorbate vibration contribution to the electronic energy, and the free energy of a molecule is calculated by adding the vibration, translation, and rotation (if applicable) contributions (calculated using Gaussian software)[48] to the electronic energy. The pH and potential effects are included using the computational hydrogen electrode model.[49] The transition state barriers were calculated using CI-NEB method.[50]

Acknowledgements

The work is supported by the Department of Energy (USA) under Award Number DE-FE0029868 and National Natural Science Foundation of China, under Award 51601030, 21773023. F.J., W.L, J.J.L, M.J., and B.H.K also thank the National Science Foundation Faculty Early Career Development program (Award No. CBET-1350911). Y.J.K. and X.B.F. acknowledge the support from International Institute for Nanotechnology (IIN) and Institute for Sustainability and Energy (ISEN) at Northwestern University. The theoretical calculation is the supported by Welch Foundation (Grant No. F-1959-20180324) and the startup grant from UT Austin, and used computational resources sponsored by the DOE's Office of Energy Efficiency and Renewable Energy and located at the National Renewable Energy Laboratory, and the Texas Advanced Computing Center (TACC) at UT Austin. This work made use of the Electron Probe Instrumentation Center (EPIC) facility of Northwestern University's Atomic and Nanoscale Characterization Experimental Center (NUANCE), which has received support from the Soft and Hybrid Nanotechnology Experimental (SHyNE) Resource (NSF ECCS-1542205); the Materials Research Science and Engineering Centers (MRSEC) program (NSF DMR-1121262) at the Materials Research Center; the IIN. This work made use of the J.B. Cohen X-Ray Diffraction Facility supported by MRSEC and SHyNE. The authors acknowledge Dr. Dong Su (Brookhaven National Laboratory), Prof. Xingchen Ye (Indiana University), and Prof. Amanda Petford-Long (Northwestern University) for help in discussion. This research used resources at the 8-ID Beamline of the National Synchrotron Light Source II, a U.S. Department of Energy (DOE) Office of Science User Facility operated for the DOE Office of Science by Brookhaven National Laboratory under Contract No. DE-SC0012704. The authors acknowledge Dr. Eli Stavitski (8-ID Beamline, NSLS-II, Brookhaven National Laboratory) for assistance in XAS measurements.

Author contributions

Y.J.K. and F.J. conceived the idea and supervised the project. X.B.F. designed the catalyst and synthesized the Cu nanomaterials. W.L. performed the electrocatalytic studies. Y.J.K., X.B.F., W.L., Y.Y.L., and F.J. analysed data and drafted the manuscript. J.J.L. and M.J, performed the electrocatalytic study on Cu nanoparticles and micron-sized particles. M.J. designed the *operando* XAS flow-cell electrolyzer, and M.J., B.H.K., and W.L. performed the XAS study. Y.B.X., X.B.H. and J.S.W. facilitated the electron microscopic work. Q.T. assisted the AFM measurement. J.J.S. and Y.Y.L. performed the computational modelling studies. All the authors contributed to discussion of the results and manuscript preparation. W. L. and X.B.F. contributed equally to this work and each of them has the right to list themselves first in the bibliographic documents.

References

1 Zhuang, T.-T. *et al.* Steering post-C–C coupling selectivity enables high efficiency electroreduction of carbon dioxide to multi-carbon alcohols. *Nat. Catal.* **1**, 421-428, (2018).

2 Ripatti, D. S., Veltman, T. R. & Kanan, M. W. Carbon Monoxide Gas Diffusion Electrolysis that Produces Concentrated C_2 Products with High Single-Pass Conversion. *Joule* **3**, 240-256, (2018).

3 Jouny, M., Luc, W. & Jiao, F. High-rate electroreduction of carbon monoxide to multi-carbon products. *Nat. Catal.* **1**, 748-755, (2018).

4 Jiang, K. *et al.* Metal ion cycling of Cu foil for selective C–C coupling in electrochemical CO_2 reduction. *Nat. Catal.* **1**, 111-119, (2018).

5 Dinh, C.-T. *et al.* CO_2 electroreduction to ethylene via hydroxide-mediated copper catalysis at an abrupt interface. *Science* **360**, 783, (2018).

6 De Luna, P. *et al.* Catalyst electro-redeposition controls morphology and oxidation state for selective carbon dioxide reduction. *Nat. Catal.* **1**, 103-110, (2018).

7 Ma, S. *et al.* Electroreduction of Carbon Dioxide to Hydrocarbons Using Bimetallic Cu–Pd Catalysts with Different Mixing Patterns. *J. Am. Chem. Soc.* **139**, 47-50, (2017).

8 Lu, Q. *et al.* A selective and efficient electrocatalyst for carbon dioxide reduction. *Nat. Commun.* **5**, 3242, (2014).

9 Li, C. W., Ciston, J. & Kanan, M. W. Electroreduction of carbon monoxide to liquid fuel on oxide-derived nanocrystalline copper. *Nature* **508**, 504, (2014).

10 Jouny, M., Luc, W. & Jiao, F. General Techno-Economic Analysis of CO_2 Electrolysis Systems. *Ind. Eng. Chem. Res.* **57**, 2165-2177, (2018).

11 Lv, J.-J. *et al.* A Highly Porous Copper Electrocatalyst for Carbon Dioxide Reduction. *Adv. Mater.* **0**, 1803111, (2018).

12 Raciti, D., Livi, K. J. & Wang, C. Highly Dense Cu Nanowires for Low-Overpotential CO_2 Reduction. *Nano Lett.* **15**, 6829-6835, (2015).

13 Hori, Y., Wakebe, H., Tsukamoto, T. & Koga, O. ELECTROCATALYTIC PROCESS OF CO SELECTIVITY IN ELECTROCHEMICAL REDUCTION OF CO_2 AT METAL-ELECTRODES IN AQUEOUS-MEDIA. *Electrochim. Acta* **39**, 1833-1839, (1994).

14 Kuhl, K. P., Cave, E. R., Abram, D. N. & Jaramillo, T. F. New insights into the electrochemical reduction of carbon dioxide on metallic copper surfaces. *Energy Environ. Sci.* **5**, 7050-7059, (2012).

15 Kuhl, K. P. *et al.* Electrocatalytic Conversion of Carbon Dioxide to Methane and Methanol on Transition Metal Surfaces. *J. Am. Chem. Soc.* **136**, 14107-14113, (2014).

16 Hori, Y., Takahashi, R., Yoshinami, Y. & Murata, A. Electrochemical reduction of CO at a copper electrode. *J. Phys. Chem. B* **101**, 7075-7081, (1997).

17 Yang, H.-J., He, S.-Y., Chen, H.-L. & Tuan, H.-Y. Monodisperse Copper Nanocubes: Synthesis, Self-Assembly, and Large-Area Dense-Packed Films. *Chem. Mater.* **26**, 1785-1793, (2014).

18 Jin, M. *et al.* Shape-Controlled Synthesis of Copper Nanocrystals in an Aqueous Solution with Glucose as a Reducing Agent and Hexadecylamine as a Capping Agent. *Angew. Chem. Int. Ed.* **50**, 10560-10564, (2011).

19 Huang, J. F. *et al.* Potential-induced nanoclustering of metallic catalysts during electrochemical CO_2 reduction. *Nat. Commun.* **9**, 3117, (2018).

20 Guo, H. Z. *et al.* Shape-Selective Formation of Monodisperse Copper Nanospheres and Nanocubes via Disproportionation Reaction Route and Their Optical Properties. *J. Phys. Chem. C* **118**, 9801-9808, (2014).

21 Salzemann, C., Urban, J., Lisiecki, I. & Pileni, M. P. Characterization and Growth Process of Copper Nanodisks. *Adv. Funct. Mater.* **15**, 1277-1284, (2005).

22 Tao, F. *et al.* Break-Up of Stepped Platinum Catalyst Surfaces by High CO Coverage. *Science* **327**, 850, (2010).

23 Tao, F. *et al.* Reaction-Driven Restructuring of Rh-Pd and Pt-Pd Core-Shell Nanoparticles. *Science* **322**, 932-934, (2008).

24 Verma, S. *et al.* Insights into the Low Overpotential Electroreduction of CO_2 to CO on a Supported Gold Catalyst in an Alkaline Flow Electrolyzer. *ACS Energy Lett.* **3**, 193-198, (2018).

25 Zhuang, T.-T. *et al.* Copper nanocavities confine intermediates for efficient electrosynthesis of C3 alcohol fuels from carbon monoxide. *Nat. Catal.* **1**, 946-951, (2018).

26 Ma, S. C. *et al.* One-step electrosynthesis of ethylene and ethanol from CO_2 in an alkaline electrolyzer. *J. Power Sources* **301**, 219-228, (2016).

27 Weekes, D. M., Salvatore, D. A., Reyes, A., Huang, A. X. & Berlinguette, C. P. Electrolytic CO_2 Reduction in a Flow Cell. *Acc. Chem. Res.* **51**, 910-918, (2018).

28 Dunwell, M., Luc, W., Yan, Y. S., Jiao, F. & Xu, B. J. Understanding Surface-Mediated Electrochemical Reactions: CO_2 Reduction and Beyond. *ACS Catal.* **8**, 8121-8129, (2018).

29 Lum, Y. W., Cheng, T., Goddard, W. A. & Ager, J. W. Electrochemical CO Reduction Builds Solvent Water into Oxygenate Products. *J. Am. Chem. Soc.* **140**, 9337-9340, (2018).

30 Liu, X. Y. *et al.* pH effects on the electrochemical reduction of CO_2 towards C_2 products on stepped copper. *Nat. Commun.* **10**, 32, (2019).

31 Wang, L. *et al.* Electrochemical Carbon Monoxide Reduction on Polycrystalline Copper: Effects of Potential, Pressure, and pH on Selectivity toward Multicarbon and Oxygenated Products. *ACS Catal.* **8**, 7445-7454, (2018).

32 Strmcnik, D. *et al.* Improving the hydrogen oxidation reaction rate by promotion of hydroxyl adsorption. *Nat. Chem.* **5**, 300-306, (2013).

33 Raciti, D. *et al.* Low-Overpotential Electroreduction of Carbon Monoxide Using Copper Nanowires. *ACS Catal.* **7**, 4467-4472, (2017).

34 Droog, J. M. M. & Schlenter, B. OXYGEN ELECTROSORPTION ON COPPER SINGLE-CRYSTAL ELECTRODES IN SODIUM-HYDROXIDE SOLUTION. *J. Electroanal. Chem.* **112**, 387-390, (1980).

35 Schouten, K. J. P., Gallent, E. P. & Koper, M. T. M. Structure Sensitivity of the Electrochemical Reduction of Carbon Monoxide on Copper Single Crystals. *ACS Catal.* **3**, 1292-1295, (2013).

36 Hahn, C. *et al.* Engineering Cu surfaces for the electrocatalytic conversion of CO_2: Controlling selectivity toward oxygenates and hydrocarbons. *Proc. Natl. Acad. Sci. U.S.A.* **114**, 5918-5923, (2017).

37 Cheng, T., Xiao, H. & Goddard, W. A. Full atomistic reaction mechanism with kinetics for CO reduction on Cu(100) from ab initio molecular dynamics free-energy calculations at 298 K. *Proc. Natl. Acad. Sci. U.S.A.* **114**, 1795-1800, (2017).

38 Cheng, T., Xiao, H. & Goddard, W. A. Nature of the Active Sites for CO Reduction on Copper Nanoparticles; Suggestions for Optimizing Performance. *J. Am. Chem. Soc.* **139**, 11642-11645, (2017).

39 Xiao, H., Cheng, T., Goddard, W. A. & Sundararaman, R. Mechanistic Explanation of the pH Dependence and Onset Potentials for Hydrocarbon Products from Electrochemical Reduction of CO on Cu (111). *J. Am. Chem. Soc.* **138**, 483-486, (2016).

40 Calle-Vallejo, F. & Koper, M. T. M. Theoretical Considerations on the Electroreduction of CO to C_2 Species on Cu(100) Electrodes. *Angew. Chem. Int. Ed.* **52**, 7282-7285, (2013).

41 Chen, C. *et al.* Highly Crystalline Multimetallic Nanoframes with Three-Dimensional Electrocatalytic Surfaces. *Science* **343**, 1339-1343, (2014).

42 Ravel, B. & Newville, M. ATHENA, ARTEMIS, HEPHAESTUS: data analysis for X-ray absorption spectroscopy using IFEFFIT. *J. Synchrotron Radiat.* **12**, 537-541, (2005).

43 Kresse, G. & Furthmüller, J. Efficient iterative schemes for ab initio total-energy calculations using a plane-wave basis set. *Phys. Rev. B* **54**, 11169-11186, (1996).

44 Kresse, G. & Hafner, J. Ab initio molecular dynamics for liquid metals. *Phys. Rev. B* **47**, 558-561, (1993).

45 Kresse, G. & Joubert, D. From ultrasoft pseudopotentials to the projector augmented-wave method. *Phys. Rev. B* **59**, 1758-1775, (1999).
46 Perdew, J. P., Burke, K. & Ernzerhof, M. Generalized Gradient Approximation Made Simple. *Phys. Rev. Lett.* **77**, 3865-3868, (1996).
47 Monkhorst, H. J. & Pack, J. D. Special points for Brillouin-zone integrations. *Phys. Rev. B* **13**, 5188-5192, (1976).
48 Scott, A. P. & Radom, L. Harmonic Vibrational Frequencies: An Evaluation of Hartree−Fock, Møller−Plesset, Quadratic Configuration Interaction, Density Functional Theory, and Semiempirical Scale Factors. *J. Phys. Chem.* **100**, 16502-16513, (1996).
49 Peterson, A. A., Abild-Pedersen, F., Studt, F., Rossmeisl, J. & Nørskov, J. K. How copper catalyzes the electroreduction of carbon dioxide into hydrocarbon fuels. *Energy Environ. Sci.* **3**, 1311-1315, (2010).
50 Henkelman, G., Uberuaga, B. P. & Jonsson, H. A climbing image nudged elastic band method for finding saddle points and minimum energy paths. *J. Chem. Phys.* **113**, 9901-9904, (2000).

Competing interests

The authors declare no competing interests.

Data availability

The datasets generated during and/or analysed during the current study are available from the corresponding authors on reasonable request.

Table of Content Figure